Elastography of multicellular aggregates submitted to osmo-mechanical stress

Charles-Edouard Leroux, Joelle Palmier, Albert-Claude Boccara, Giovanni Cappello, Sylvain Monnier

Elastography of multicellular aggregates submitted to osmo-mechanical stress

2015 New J. Phys. 17 073035

(http://iopscience.iop.org/1367-2630/17/7/073035)

New Journal of Physics
The open access journal at the forefront of physics

Deutsche Physikalische Gesellschaft DPG
IOP Institute of Physics

Published in partnership with: Deutsche Physikalische Gesellschaft and the Institute of Physics

OPEN ACCESS

RECEIVED
24 March 2015

REVISED
17 June 2015

ACCEPTED FOR PUBLICATION
3 July 2015

PUBLISHED
31 July 2015

PAPER

Elastography of multicellular aggregates submitted to osmo-mechanical stress

Charles-Edouard Leroux[1], Joelle Palmier[1], Albert Claude Boccara[1], Giovanni Cappello[2] and Sylvain Monnier[3]

[1] ESPCI ParisTech, PSL Research University, CNRS, Institut Langevin, 1 rue Jussieu, F-75005 Paris, France
[2] Univ. Grenoble Alpes, LIPHY, F-38000 Grenoble, France
[3] Physicochimie Curie (Institut Curie/CNRS-UMR168/UPMC), Institut Curie, Centre de Recherche, 26 rue dUlm, F-75248 Paris Cedex 05, France

E-mail: charles-edouard.leroux@espci.fr, eaplister@gmail.com, claude.boccara@espci.fr, giovanni.cappello@ujf-grenoble.fr and sylvain.monnier@curie.fr

Keywords: mechanical properties of tissues, optical coherence tomography, cell dynamics

Abstract

Tumors are subjected to mechanical stress generated by their own growth in a confined environment, and by their surrounding tissues. Recent works have focused on the study of the growth of spherical aggregates of cells, spheroids, under controlled confinement or stress. In this study we demonstrate the measurement of spatially and temporally resolved deformation maps inside spheroids while applying an osmo-mechanical stress. We use full field optical coherence tomography, a high resolution imaging technique well suited for real-time measurements of deformation in living tissues under stress. Using the spherical symmetry of the experiment, we compare our data to a mechanical modeling of the spheroid as a continuous medium. We estimate the viscoelastic parameters of spheroids and discuss the apparent tissue anisotropy after the osmo-mechanical stress.

1. Introduction

A tumor mechanically interacts with its surrounding tissue, the stroma. *In vitro*, unbounded growth of cancerous cells can exert pushing forces and compress the tumor surroundings [1]. *In vivo*, tumor growth-induced stress can impact the tumor micro-environment [2] and can eventually promote cancer progression in a confined environment [3]. How a tumor responds, at the cellular level, to mechanical constraints is still an open question. Beside their clinical relevance, mechanical properties of tissues or cells play important roles in basic biological processes such as differentiation [4], morphogenesis [5] and cancer invasion [6, 7].

Spheroids are spherical cellular aggregates commonly used to mimic pre-vascularized tumors *in vitro*. They are usually built by the aggregation of a single type of cells. Like cells cultured on a flat substrate, they are a valuable tool for drug screening, or designing well controlled biophysical experiments [8]. In fact, their overall simple spherical geometry generates a radial gradient in oxygen, nutrients, and drug penetration and make them a valuable tool for anti-cancer drug screening [9]. Various methods have been presented to study the effect of biologically viable stress on the growth of spheroids, without perturbing vital exchanges of oxygen and nutrients with the culture medium: growth in stressed agarose gels [1], within hydrogel capsules [7], or under osmo-mechanical pressure [10]. These experiments show that pressure or confinement impedes spheroid growth by inhibiting proliferation of cells preferentially located in the inner layers [1, 10], but can also trigger invasion of the surrounding environment [7].

Osmo-mechanical stress provide an elegant and easy way to apply isotropic stress to a spherical cell aggregate [10, 11]. The stress can indeed be generated by simply adding a biopolymer to the culture medium, without major perturbation at the cellular levels. Large molecules of dextran, in the order of 100 kDa, do not penetrate inside the aggregate, so that the peripheral cellular layers acts as an impermeable membrane and transmit an isotropic stress to the spheroid [11]. Recently, it was observed such a pressure reduces the aggregate growth by

inhibiting proliferation of cells located in the inner layers of the aggregate [10, 11]. This spatial inhomogeneity in the response to an osmo-mechanical stress is thought to emerge from the stress distribution inside the aggregate, as an important compression at the center of the spheroid (60% in volume) was reported 5 min after pressure application, while the volume of peripheral cells seems not to be affected [12].

Over shorter timescales (minutes), the mechanical properties of a spheroid are those of a passive, viscoelastic material. Numerous experimental methods based on pure mechanical perturbations have been introduced to characterize the viscoelastic behavior of cellular aggregates [13]. Indeed, mechanical properties such as Young's modulus, viscosity or surface tension were extracted from parallel plates experiments historically introduced by Steinberg and co-workers [14–16], spheroid centrifugation [17], or micropipette aspiration [18]. The later study interestingly showed that the surface tension depends on the applied stress, suggesting an active reaction of the cell to mechanical constraints[18]. Spheroid grown under confinement between PDMS walls exhibited plastic behavior after constraint release, this shows that long-term stress can also modify the mechanical properties of such systems [19].

In order to understand the growth impediment of spheroids submitted to dextran-generated osmo-mechanical stress, we use full field optical coherence tomography (FFOCT) to characterize the rapid response of cellular aggregates to such a compressive stress. Low coherent interferometric imaging techniques, such as digital holography [20–22] and point scanning optical coherence tomography [23, 24], have a great potential to study cell dynamics in living tissues. At an improved isotropic resolution of around 1 μm (versus 10 μm for the mentioned techniques), FFOCT provides 2D images with a contrast that is due to the light locally back-scattered from the sample, which interferes with a reference beam. Thus, no prior staining with dyes is needed. As an interferometric imaging technique, FFOCT is extremely sensitive to sub-micron deformation of biological tissues, and is therefore well suited to perform real-time elastography of biological tissues [25–27]. Elastography is a technique that was first developed for ultrasound imaging, in order to add a stiffness contrast to standard images by measuring the local displacement in a tissue under dynamic or static mechanical excitation.

Here, we measure the compression in real time on living spheroids and use a recently proposed [28] mechanical modeling of the spheroid as a continuous medium to interpret quantitatively the spatio-temporal behavior of the measured deformation. First, we exclude any potential artifact due to the cryosection process in previous work [28]. Second, we dynamically measure the compression field as a function of the time. Our experimental data confirm that the response of a spheroid to a mechanical perturbation deviates from what is expected for a homogeneous isotropic sphere and confirms, with real-time measurements inside living spheroids, that a radial gradient in volumetric compression builds up in the core of the spheroid within minutes after the pressure jump.

2. Methods

2.1. Imaging using FFOCT

With FFOCT, the coherent back-scattered signal is isolated from the background by phase modulation of the reference beam, which allows deep imaging inside thick biological tissues that scatter light. The positive contrast originates from the local change of refractive index introduced by the cell membrane. The low coherence of the light source, in combination with adequate optical filters, sets the sectioning power of the microscope to approximately 1 μm along the optical axis. This value matches the transverse resolution of the microscope, which is set by the numerical aperture of the microscope objectives.

The FFOCT images were recorded using a commercial microscope (Light-CT, LLTECH, Paris, France) with a CMOS camera (MV-D1024E, Photonfocus) and a halogen lamp (KL 1500 compact, Schott). We show in figure 1 the schematic of the optical layout of the microscope, which can be thought as a Michelson interferometer with identical objectives in the reference and sample arm. With an irradiance as low as 2 mW mm^{-2} on the sample, the signal to noise ratio of a single FFOCT image is around 2 at the surface of the spheroid (acquired at 25 Hz), and typically drops to a value of 0.5 at a 100 μm imaging depth because of light scattering and optical aberrations. We found that imaging at a 100 μm depth inside spheroids of radius 200 microns was a good compromise to obtain good quality images for the time-resolved measurements of local displacement. Each processed FFOCT image is the average of 100 accumulated frames, so that the displacements are computed with a 4 s temporal resolution. The accumulation of a larger number of frames is beneficial to see with clarity the cellular contour with a negative contrast. In figure 2.1, we show the FFOCT image of a spheroid section at the 100 μm depth after accumulating 1000 frames (40 s acquisition time). Inside the cells, organelles are barely visible on the FFOCT images because they introduce very little change of refractive index, and their temporal dynamics reduce the OCT signal for acquisition times larger than 1s [24].

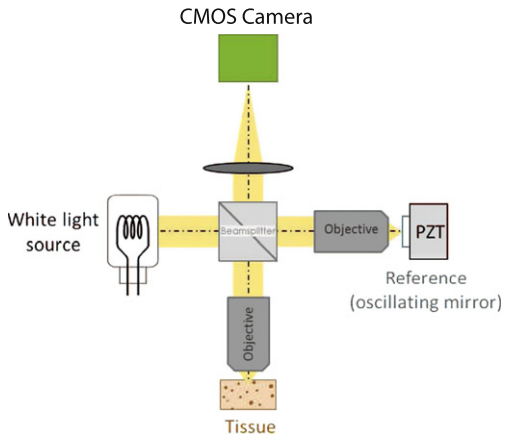

Figure 1. Optical layout of the full-field optical coherence tomography setup (FFOCT). As for standard OCT, the low coherence of the light source allows the sectioning of thin (0.8 μm) slices of diffusers inside thick biological tissues. Koehler illumination of the sample allows the parallel acquisition of around 1 million CMOS pixels, as in a standard wide-field microscope.

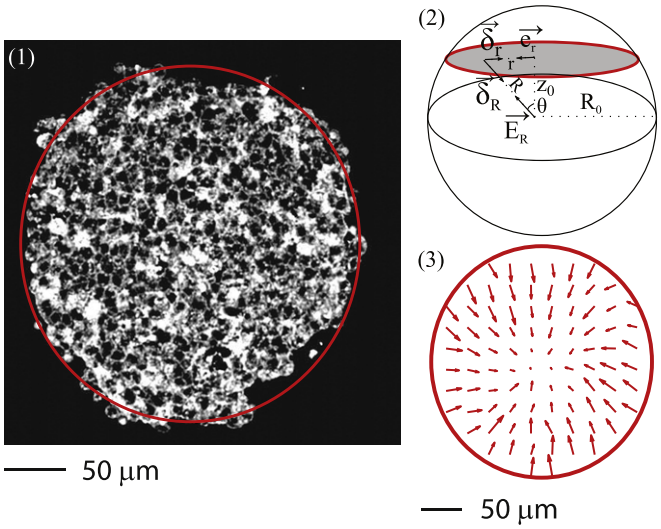

Figure 2. (1) FFOCT image of a living CT26 spheroid at a 100 μm imaging depth. The FFOCT signal is acquired for 40 s and reveals boundaries of individual cells (white). No staining is required to obtain the contrast. (2) Geometry and notations: the gray slice is the observation plane, located at a distance $z_0 = R_0/2$ from the spheroid center. $\vec{\delta}_R$ is the 3D displacement, and $\vec{\delta}_r$ its measured 2D projection. R and r are the radial coordinates relative to the spheroid center and the image and image respectively. (3) Displacement field $\vec{\delta}_r$ integrated over 4 min after a 10 kPa pressure jump (displayed with a 10 times scaling factor for visibility purpose). The displacements are estimated every 25 μm with a 20 nm precision.

2.2. FFOCT-based elastography

FFOCT is a coherence-based imaging technique, which provides a mapping of the back-scattered optical field both in phase and amplitude. The system was used here in amplitude mode, and therefore provides a spatial mapping of reflectivity inside the spheroid. In such an amplitude mode, scanning (non-full field) OCT systems have been extensively used to map the axial displacement inside tissues under static load by computing the spatial cross-correlation of successive cross-sections (xz images, or 'B-scan' [27]). We use a similar approach, the difference being that the internal displacements are estimated in 2D from successive en-face (xy) images. The spatial resolution is improved 10 times with our full-field approach of OCT [29]. We estimate the in-plane displacement field at the position $\vec{r}$ by computing the position of the maximum of the 2D cross-correlation function of a small ($N \times N$ pixels, with $N = 32$) portion of the FFOCT images at two consecutive acquisition times. This correlative method is accurate for displacements smaller than the resolution limit of the microscope (0.8 μm), and requires to use of a portion large enough to reduce computational errors [27, 30–33]. Here we choose a conservative $N = 32$ pixel window size, which also sets the spatial resolution of the displacement map. The measured displacement between consecutive frames is only a fraction of pixels, and become significantly larger than the noise (1/20 pixel) after spatio-temporal averaging. We integrate the displacement over time to

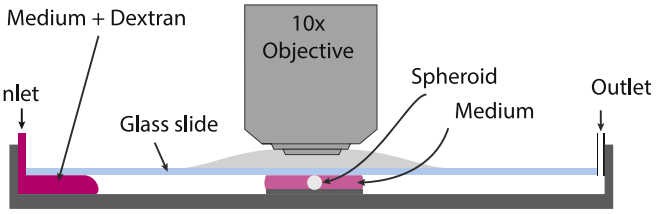

Figure 3. Schematic of the experiment, showing the side inlet for adding dextran in the culture medium while imaging with FFOCT.

obtain the cumulative displacement field $\vec{\delta}_r(t)$ in the sectioned plane. As a result of the compressive stress, $\vec{\delta}_r(t)$ points towards the center of the section of the spheroid. It has a negative projection over the unitary vector $\vec{e}_r$, as defined by figure 2.2. We show in figure 2.3 $\vec{\delta}_r$, 4 min after the 10 kPa pressure jump of a CT26 spheroid. Note that the arrows have been magnified by 10 for visual clarity. On overall the accumulated displacements show a radial symmetry, and are in the order of 1 μm, which is much smaller than the spatial windowing of 25 μm used for their calculation. Imaging is performed at a distance $z_0 = R_0/2$ from the spheroid center so by geometrical projection one can get the cumulative displacement in the equatorial plane of the spheroid $\vec{\delta}_R(t)$. Figure 2.2 summarizes the geometry and the notations used in the manuscript.

Thanks to the geometry of the experiment, the out of plane displacements are small. They are larger at the center of the field of view of the FFOCT images (around 1μm of accumulated axial displacements at the end of the experiment, for the larger pressure jumps). Such axial displacements are marginalized by a geometrical projection of the measurements, as detailed in section 3. In some rare occasions they have a negative effect on the estimation of the in-plane displacements, when they induce a change between two consecutive sub-images. This can occur when imaging the apex of a cell, but it is a very rare event as the accumulated axial displacement ($\simeq$1μm) is in the order of the axial resolution of the microscope. Alternatively, we could measure out of plane displacements with a 3D correlative approach, at the cost of a major reduction in temporal sampling. Doing so would require the acquisition of 3D stacks of images for each measurement time, so that each processed image is a cube of size $N \times N \times N$. Recently, our group demonstrated the potential of Full-Field OCT to obtain 3 D displacement field after a static load [25].

2.3. Spheroid preparation

Spheroids were prepared with either mouse (CT26) or human colon carcinoma (HT29) cells, following a cushion agarose protocol [34] and were cultured at 37 °C with 5% CO_2 in Dulbeccos modified medium (DMEM, Life Technologies) supplemented with 10% fetal bovine serum (Life Technologies) and 1% penicillin/streptomycin (Life Technologies). The experiments were performed 3 days after the formation of the spheroid, so that there was no necrotic core due to poor diffusion of oxygen and nutrients. Moreover, the small size of the spheroids ($R_0 \simeq 200\,\mu$m) reduces most of the relevant biophysical gradients that are conventionally observed 5-10 days after the complete build up [9].

2.4. Pressure clamp experiment

Dextran is a biocompatible polymer that does not enter the cells nor the aggregate, and therefore applies a controlled mechanical stress from the outer layer of the aggregate [11]. The relationship between the osmotic pressure and the concentration of dextran was calibrated with light scattering by Bonnet-Gonnet *et al* [35]. Imaging was performed in a 100 μL volume of culture medium before and after injection of large volume (1mL, injected in less than 20 s of medium supplemented with 100 kDa dextran (Sigma Aldrich, St Louis, USA). Spheroids were carefully inserted between the substrate and a glass slide to prevent them from moving during the injection (figure 3), so that no measurable compression by the plate was observed prior dextran injection.

2.5. Spatial averaging

The contrast originating from the cell membrane allows us to track cell boundaries within the aggregate from which we extract the displacement profiles for three amplitudes of pressure jumps and two cell lines. From the FFOCT images we extract a two dimensional displacement field $\vec{\delta}_r(\vec{r}, t)$. To reduce the impact of the measurement noise, we take into account the spherical symmetry of the experiment and spatially average its radial component $\delta_r^i(t) = -\langle \vec{\delta}_r(t) \cdot \vec{e}_r \rangle_i$ over three separate regions that contain the same number of measurement points (20) in the FFOCT image : a peripheral ring (of mean radius $r_1 = 155\,\mu$m), an intermediate ring ($r_2 = 112\,\mu$m) and a central disk ($r_3 = 60\,\mu$m). The negative sign gives positive values for $\delta_r^i(t)$, as a result of compression. Each region corresponds to one third of the total number of measurements. They correspond to

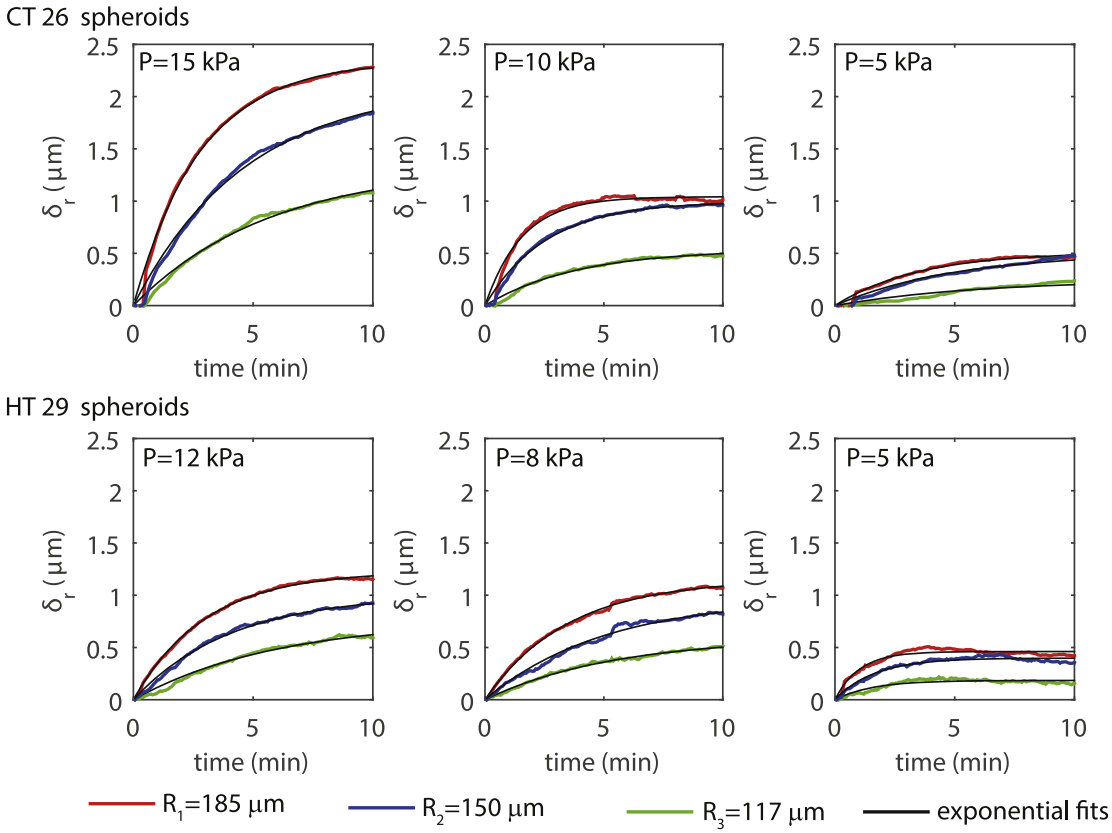

Figure 4. Radial component of the 2D measured displacement field, $\delta_r(\vec{r}, t)$, spatially integrated over three regions of the FFOCT en-face images (1/3 of the measurement points each). Green: central disk. Blue: intermediate annulus. Red: external annulus. Black curves are single exponential fits.

mean radial positions of $R_1 = 185 \pm 18\,\mu$m, $R_2 = 150 \pm 18\,\mu$m, and $R_3 = 117 \pm 18\,\mu$m relative to the center of the spheroid.

We compute the local volumetric compression inside the spheroid from the radial displacements. To do so, we consider the spheroid as a continuous medium, where the radial displacements and the volumetric compression are locally related by spatial differentiation. Appendix 1 details these calculations. As the FFOCT images mostly contain information about the cellular contour and the spheroid has a spherical symmetry, we consider that this volumetric compression is the cell compression. We obtain two time series $-\left(\frac{dV}{V}\right)_{i|j}(t)$, which are time-resolved measurements of the volumetric compression at the positions $R_{1|2}$ and $R_{2,3}$ from the center of the spheroid. These positions correspond to the interfaces of the sub-regions used for spatial averaging : $R_{1|2} = 170\,\mu$m ($\simeq(R_1 + R_2)/2$) and $R_{2|3} = 135\,\mu$m ($\simeq(R_2 + R_3)/2$). As a result of the compressive stress, $-\left(\frac{dV}{V}\right)_{i|j}(t)$ is a positive measurement that locally quantifies the relative reduction of cell volume.

3. Results and discussion

3.1. Spatial averaging

Displacements for the three radii in the spheroid display an exponential behavior $\delta_r(t) = \delta_r(1 - e^{-t/\tau})$, as shown in figure 4. The amplitude δ_r is proportional to the intensity of the stress (figure 5.1), and is more important at the periphery of the spheroids.

Cells start moving immediately after the pressure jump independently of the pressure applied, but the velocity is smaller for the cells inside the aggregate as shown by the relaxation times τ in figure 5.2. This accounts for the viscous behavior of the aggregate, the τ is in the order of minutes as already shown in [16] with parallel plate compression.

The volumetric compression $-\left(\frac{dV}{V}\right)_{i|j}(t)$ is a positive quantity, as a result of the compressive stress. At the end of our experiment ($t = 10$ min), the volumetric compression for the cells in the outer region is in the order of 5% (figure 5.3), as expected from purely osmotic shock on single cell experiments [36]. The compression is

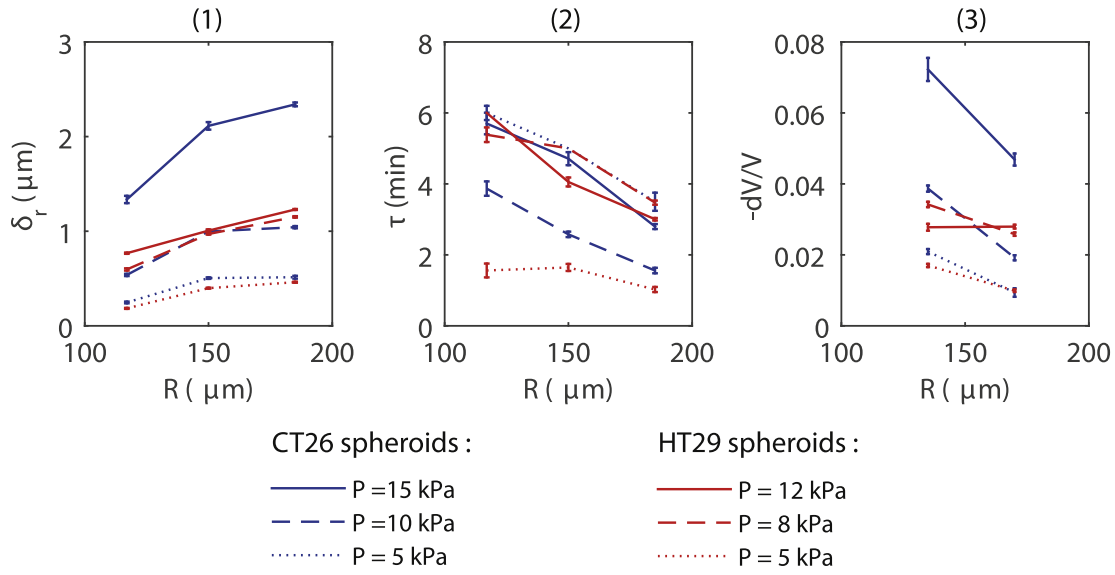

Figure 5. Spatially-averaged data as a function of the radial position R relative to the spheroid center : (1) radial displacements accumulated over the 10 min of the experiment, (2) characteristic times τ of the radial displacement. (3) Volumetric compression 10 min after the pressure jump, computed using equation (6).

higher for the inner cells of the CT26 spheroids, which confirms the observation made by Delarue *et al* on fixed samples of the same cell line [12]. They measured the cell–cell distance as a function of the distance to the center in equatorial cryosections of spheroids. In the context of continuous mechanics, cell to cell distance is related to the local cell density and volumetric compression of the spheroid. Their observation were performed on fixed aggregates, 5 min after a 5–10 kPa osmo-mechanical pressure jump, while we provide here a time-resolved observation of the gradient in compression on living spheroids. Figure 6 show the volumetric compression $-\left(\frac{\mathrm{d}V}{V}\right)_{i|j}(t)$. The radial gradient of compression is less obvious with HT29 cells as the displacements are smaller and our measurements were not performed in the equatorial section of the spheroid. Indeed, the radial averaging for the volume compression calculation lead to a loss of information. In the next section, we use a model-based analysis to better capture the dynamic response of the spheroid, and especially the higher compression observed in the core of the aggregate.

3.2. Model-based analysis

Spheroids can be described at the mesoscopic scale as a continuous medium. A model was recently introduced to describe the spatio-temporal behaviors of the flow and pressure inside a spheroid under isotropic pressure [28]. Considering the cell aggregate as a viscoelastic and homogeneous material, the authors emphasized the role of anisotropic stress inside the spheroid, and write the displacement as a power-law expression. Due to spherical symmetry, the displacement is nevertheless radially oriented, and its Laplace transform writes :

$$\vec{\delta}_R(s) = -A(s) \cdot \left(\frac{R}{R_0}\right)^{1+B(s)} \vec{E}_R \tag{1}$$

with s being the inverse variable of time, R_0 is the spheroid radius, and $\vec{E}_r$ is the unitary radial vector in spherical coordinate (see figure 2.2). $A(s)$ characterizes the dynamics of compression of the spheroid as a homogeneous and isotropic sphere of bulk modulus K. It also characterizes the magnitude of displacement at the periphery of the spheroid ($R = R_0$). The $B(s)$ term is a dimensionless term that characterizes the role of anisotropic stress inside the spheroid. It is appropriate to model the anisotropic stress that appear inside the spheroid as a result of active tension generated by the cells and their change of orientation. When $B(s) = 0$, $\vec{\delta}_R(s)$ is linear in R, in this case, the spheroid behaves like a homogeneous isotropic sphere. Its dynamics is then fully characterized by $A(s)$.

It is important to stress that for the model-based analysis we work in the observation plane at the distance $z_0 = R_0/2$, where the radial position is denoted with r as opposed to R (See figure 2.2). Then equation (1) writes as function of the radial coordinate r and time :

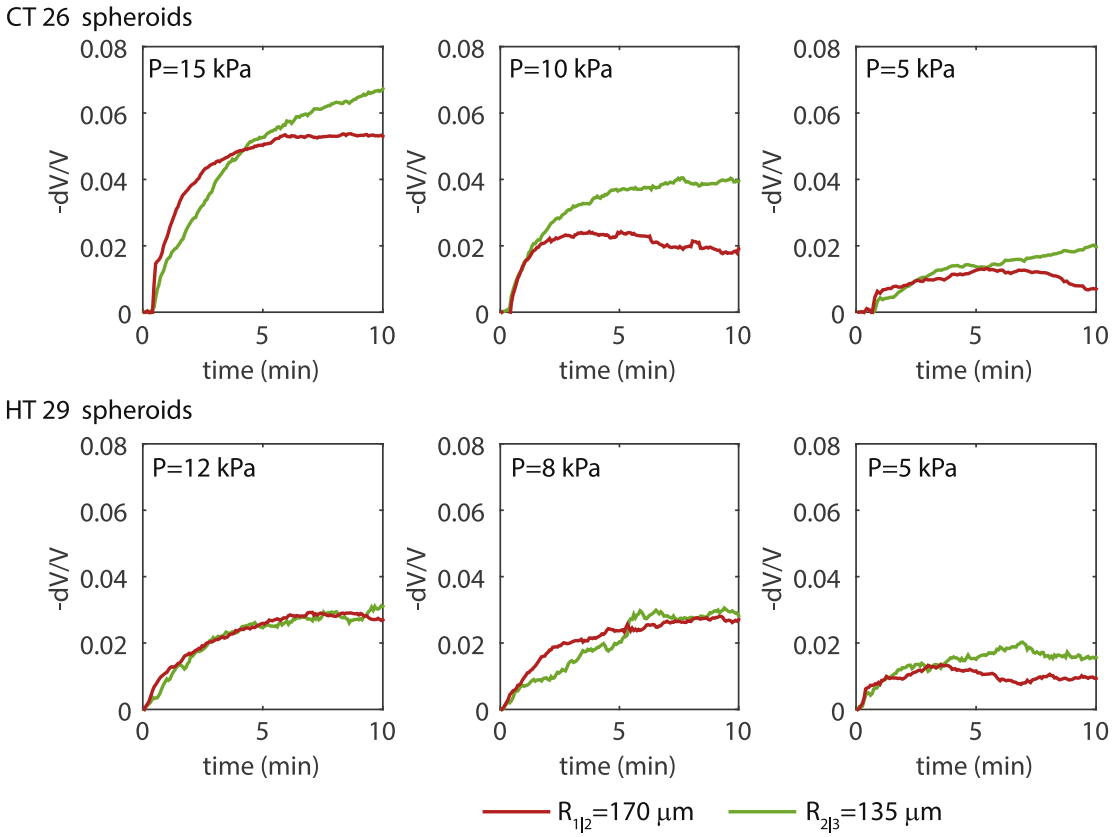

Figure 6. Time series of the volumetric compression inside the aggregates at $R_{1|2} = 170$ and $R_{2|3} = 170\,\mu$m from the center of the spheroid.

$$\vec{\delta}_r(t) \approx -\Big(\alpha(t) \cdot r/R_0 + \beta(t) \cdot f(r)\Big)\vec{e}_r, \tag{2}$$

where $f(r) = \frac{r}{2R_0} \cdot \ln\left(\frac{r^2+z_0^2}{R_0^2}\right)$. $\alpha(t)$ and $\beta(t)$ are the inverse Laplace transforms of $A(s)$ and $A(s) \cdot B(s)$ respectively. We detailed the calculations that relate equation (1) to equation (2) in appendix 2. Our data analysis consists in the joint estimation of $\alpha(t)$ and $\beta(t)$, which are at given t the least square solutions of a linear system that implicitly project the displacement field $\vec{\delta}_r(t)$ on two radially symmetric vectors $(r/R_0)\vec{e}_r$ and $f(r)\vec{e}_r$. The sign convention of equation (2) gives $\alpha(t) > 0$ for a compression in the spheroid. For the homogeneous and isotropic sphere, $\beta(t) = 0$ and the projected displacement $\delta_r(t)$ is linear in r. We can already notice that $f(r)$ is negative in the observation plane ($0 < r < \sqrt{3}/2R_0$, for $z = R_0/2$), so that the sign of $\beta(t)$ defines the type of deviation from this simple model : whether the inner cells have moved more ($\beta(t) < 0$) or less ($\beta(t) > 0$) than expected for the homogeneous and isotropic sphere, at a given time t after the pressure jump.

3.3. $\alpha(t)$ response of the spheroid, as a homogeneous and isotropic sphere

$\alpha(t)$ characterizes the isotropic properties of the material. For the two cell lines and the entire pressure range, we find that $\alpha(t)$ is accurately fitted by a single exponential function $\alpha(t) = \alpha_0\left(1 - e^{-t/\tau_\alpha}\right)$ (figure 7, red and black curves for the data and the fit respectively). α_0 quantifies the overall magnitude of spheroid displacements as a homogeneous and isotropic sphere, and is proportional to the applied pressure P in the range of our experiments (figure 8.1). This linearity gives an estimate of the bulk modulus K of the spheroid under the hypothesis that the bulk modulus is much higher than the shear modulus [28] :

$$K = \frac{P \cdot R_0}{3\alpha_0}. \tag{3}$$

We found $K = 355 \pm 195$ kPa and $K = 514 \pm 180$ kPa for the CT26 and HT29 cells respectively. These values are four orders of magnitude lower than what is usually assumed for biological tissues, with a typical bulk modulus of about 10^9 Pa (close to the bulk modulus of water) [37]. This discrepancy can be explained by the fact that in our experiments, water is free to flow out of the spheroids through the extracellular matrix, so that the spheroids are compressible on larger timescales. The measured bulk moduli K are orders of magnitude larger than the reported Young's moduli of soft tissues ($E \in [10^2, 10^4]\,Pa$, [38] or spheroids [18] ($E \simeq 700$ Pa). Using

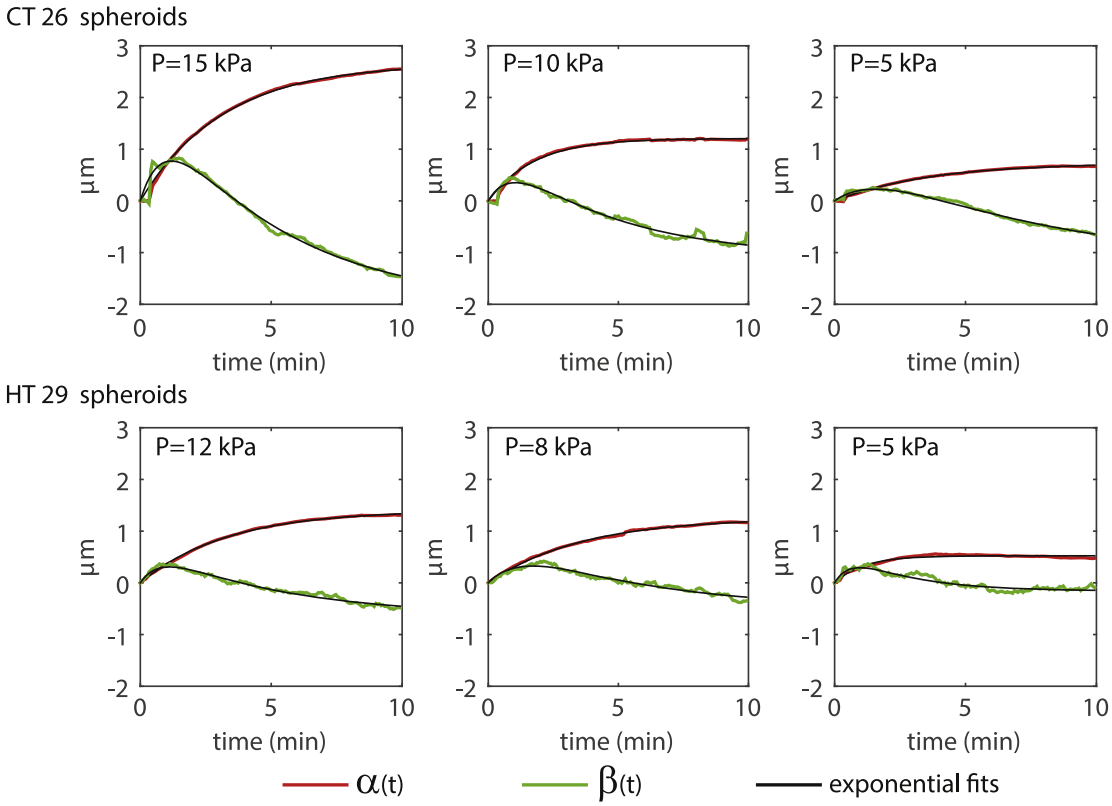

Figure 7. Time series of the estimated parameters $\alpha(t)$ (red) and $\beta(t)$ (green) for the CT26 (first row) and HT29 (second row) spheroids. $\alpha(t)$ Characterizes the spheroid displacements as a homogeneous and isotropic sphere, and $\beta(t)$ the first-order departure from this model. The black curves are exponential fits: single exponential model for $\alpha(t)$, and double exponential for $\beta(t)$ (equation (4)).

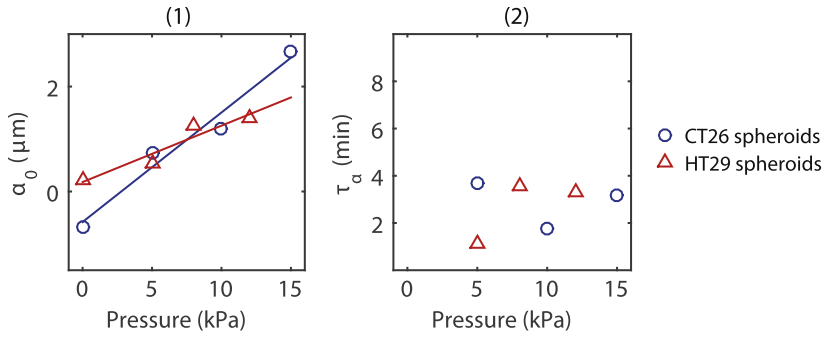

Figure 8. (1) Amplitude of the overall $\alpha(t)$ displacements up to steady state, α_0, as a function of the applied pressure P. (2) Characteristic times of $\alpha(t)$, $\tau_\alpha \simeq 3$ min. Error bars were calculated from the 95% confidence intervals of the single exponential fits, and are smaller than the plot markers. $\alpha(t)$ Characterizes the amplitude of displacement field $\vec{\delta}_r(t)$, assuming that the spheroid behaves as a homogeneous and isotropic sphere.

these typical Young's moduli we can estimate the Poisson ratio of spheroids to be very close to 0.5 ($\nu \in [0.4966,\ 0.49966]$). Spheroids are therefore very soft, mostly incompressible tissues with a shear modulus $G \simeq E/3 \ll K$. Eventually, we note that Delarue *et al*, applying similar stresses found an even smaller bulk modulus ($K = 10^4 - 10^5$) [28]. The geometries of the experiments differ : in our case the spheroid is stuck between two plates, while in their experiments the spheroid sits at the bottom of a bulk of media supplemented with dextran. In addition, whereas we perform live observations, their measurements were done after sample fixation, which could have induced artifacts.

The averaged longitudinal relaxation $\tau_\alpha \simeq 3$ min does not vary significantly with the amplitude of the external stress (figure 8.2) and is similar for the two cell lines. It is comparable to the fast component of the stress relaxation of a spheroid between parallel plates [16]. The agreement with a single exponential fit suggests that the instantaneous elastic deformation of the spheroid is small at the scale of our experiment. For comparison, at the

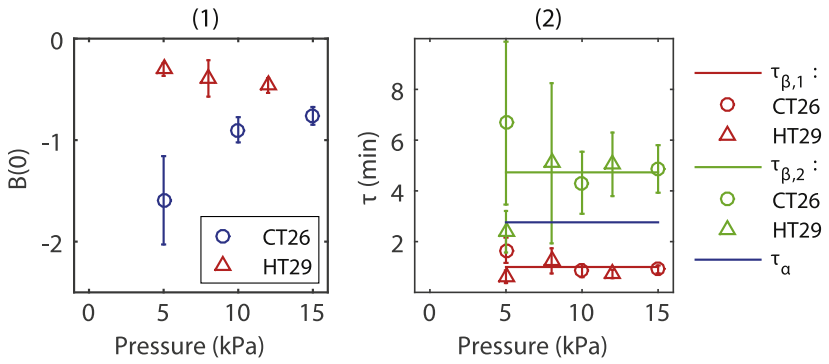

Figure 9. (1) Values B(0) of the exponent in the power law of equation (1) in the long time limit ($s = 0$) of our experiment. (2) Estimated characteristic times of $\beta(t)$, $\tau_{\beta,1}$ (red) and $\tau_{\beta,2}$ (green), which we compare to the mean value of τ_α (blue line). Error bars correspond to the 95% confidence interval of the fits.

scale of a single cell, creep experiments typically relate a fast, elastic deformation of the cell within seconds after the stress is applied [39, 40].

3.4. Departure from the homogeneous and isotropic sphere $\beta(t)$

As stated earlier, $\beta(t)$ is the deviation from the response of a homogeneous and isotropic sphere. One can observe that $\beta(t)$ is non-monotonic and appears to become negative after $\simeq$5 min for each cell line or pressure condition (green curves in figure 7). The non-zero $\beta(t)$ measurements show the significant anisotropy of a spheroid during the 10 min timescale of our experiments. The two regimes exhibited by $\beta(t)$ are empirically fitted by a sum of two exponential functions (green and black curves in figure 7), and show the multiplicity of the response to the osmo-mechanical stress:

$$\beta(t) = \beta_1\left(1 - e^{-t/\tau_{\beta,1}}\right) - \beta_2\left(1 - e^{-t/\tau_{\beta,2}}\right). \quad (4)$$

Since $f(r) < 0$, the increase of $\beta(t)$ for $t < \simeq 1$ min (figure 7) indicates that, at the beginning of the experiment, cells are resisting the dextran compression. This apparent resistance might be due to the delay previously observed in the center of the aggregate (figure 5.2). The spheroid does not compress homogeneously, since the displacements arise more slowly in the core.

The delay might correspond to the osmotic effect of the dextran, indeed, such a compression on single cells requires less than 30 s to establish (data not shown), but the osmotic equilibrium has to propagate from the outer layers to center of the aggregate. During this regime, the water flows out of the peripheral cells in the intracellular space, to finally leave the spheroid. Water diffusion through the cell membrane is probably the limiting step in this osmotic component of the reaction. If the modeling introduced by equation (1) does not explicitly take into account the dynamics of osmosis, it is interesting to note that our observation provides a time scale for the establishment of the isotropic pressure.

The second regime display an opposite reaction, $\beta(t)$ decreases and finally becomes negative. This indicates that the inner cells start moving, and they eventually move more ($\beta(t) < 0$) than what would be expected for the homogeneous and isotropic sphere of same bulk modulus. This process is slow ($\tau_{\beta,2} \simeq 4.5$ min), in comparison with the previous regime of passive response to the osmotic shock. (See figure 9.2 for comparison of the model-based characteristic times.) In their model, Delarue *et al* describe this over-reaction to the compression as an active reaction of the cell due to the establishment of an anisotropic stress within the aggregate [28].

At steady state, the exponent in the power-law of equation (1) $B(0) = (\beta_1 - \beta_2)/\alpha_0$ are negative (figure 9.1), which translates the fact that cell displacements at the center of the spheroid are, at the end of our experiment, larger than expected for an isotropic and homogeneous sphere of identical bulk modulus. Our measurements indicate that this effect is on average more important for the CT26 spheroid ($B(0) \simeq -1$) than for the HT29 spheroid ($B(0) \simeq -0.5$). Its estimation has a higher uncertainty than α_0, because i) the fit of $\beta(t)$ has more free parameters and ii) it is normalized by α_0. Negative $B(0)$ values also predict a sharp increase of compression towards the center of the spheroid at the end of our experiment, as the volumetric compression then scales as $(R/R_0)^{B(0)}$ [28]. For the HT29 cells, this increase was barely noticeable on the spatially averaged profiles of figure 5.3. Many biophysical factors can lead to this radial gradient of compression in the spheroid. Originally, the authors of the model introduced the active tension of cells in response to pressure. This active tension combined with an anisotropic orientation of the cells can thus lead to an inhomogeneous stress inside the

spheroid. On the other hand, the radial gradient of compression could also be explained by a radial inhomogeneity in cell bulk modulus within the spheroid. According to our observations, cells of the second layer would be approximately twice softer than the peripheral layer. Promising experiments to discriminate whether the active response of cells actually play a role would be to use drugs perturbing cell cortex, contractility and cell polarization.

4. Conclusion

We report the use of FFOCT to probe the mechanical properties of living cell aggregates submitted to osmo-mechanical stress. Here, we first confirm the effect on live spheroids, and second provide the timescale, for which tissue anisotropy is noticeable after an osmotic pressure jump. The spherical symmetry of the aggregates and the isotropic nature of the applied pressure allows us to apply a model-based analysis that described well our time-resolved measurements. We estimate viscoelastic parameters of the spheroid, and provide a time-resolved confirmation of an apparent tissue anisotropy within minutes after the osmotic stress is applied.

Active response of spheroid to pipette aspiration has been previously described in term of increase in surface tension whereas in our work we observe an over-reaction in the core of the aggregate [18]. This contraction is likely to originate from the cytoskeleton, and more precisely from the acto–myosin cortex [41], it will thus be interesting to test it by using drugs to inhibit myosin contraction or depolymerize actin. Modifying water transport through the cell membrane would also be a way to address the osmotic component of the contraction as the characteristic time should highly depend on it. These experiments would help distinguish between purely osmotic and mechano-osmotic response of the spheroid.

Our approach is very promising to study the mechanical behavior of spheroid over different timescale in a single experiment. We emphasized the sub-micron sensibility of FFOCT to measure displacement with a 25 μm resolution and 20 nm precision at a 100 μm imaging depth. Currently we are investigating methods to increase by a factor 2 the imaging depth of FFOCT, which would allow us to image spheroid equatorial plane and capture in real time the radial gradient of the spheroid mechanical properties. Another promising prospect of this work is to extend our cell tracking technique to prolonged experiments. As FFOCT is non-invasive at low irradiation, we believe this staining-free image method can also bring information on the long-term behavior of such systems, such as cell re-arrangements, movements or even extracellular matrix synthesis and organization.

Acknowledgments

This research is supported by the INSERM program-Physique-Mathématiques-Sciences de l'ingénieur et Cancer and the Fondation Pierre-Gilles de Gennes. We warmly thank Jacques Prost, Jean-François Joanny, and Antoine Delon for the very useful discussions and suggestions.

Appendix A.

Figure 2.2 clarifies the notations of these calculations.

A.1. Calculation of the spatially-averaged volumetric compression

In principle the displacements $\vec{\delta}_R$ and $\vec{\delta}_r$ are radially oriented, along $\vec{E}_R$ and $\vec{e}_r$ respectively (with opposite direction, see figure 2.2). Their radial components are related by $\delta_R = \delta_r/\sin(\theta)$, with $\sin(\theta) = \sin\left(\arccos(\frac{z_0}{R}\right) = \sqrt{1 - z_0^2/R^2}$. In practice we set $z_0 = R_0/2$ in this work. We measure the spatial average of δ_r over 3 sub-regions i at mean distance R_i from the center of the spheroid, $\delta_r^i(t) = -\langle\vec{\delta}_r(t)\cdot\vec{e}_r\rangle_i$ (the negative sign is introduced to show positive data in figure 4),from which we compute $\delta_R^i(t)$:

$$\delta_R^i(t) = \frac{\delta_r^i(t)}{\sqrt{1 - z_0^2/R_i^2}}. \tag{5}$$

As for δ_r, the sign convention implies that $\delta_R^i(t) > 0$ for a compressive stress.

In a spherical medium that is a radially compressed, the volumetric compression is a function of the radial displacement δ_R:

$$-\frac{\mathrm{d}V}{V} = \frac{1}{R^2}\frac{\partial}{\partial R}\left(R^2\delta_R\right). \tag{6}$$

Where $-\frac{dV}{V} > 0$ as a result of compression. We compute the volumetric compression $-\left(\frac{dV}{V}\right)_{i|j}(t)$ at the interface between the regions i and j by using equation (5) and a finite difference of equation (6):

$$-\left(\frac{dV}{V}\right)_{i|j}(t) = \frac{1}{R_{i|j}^2}\frac{R_i^2 \cdot \delta_R^i(t) - R_j^2 \cdot \delta_R^j}{R_i - R_j} \tag{7}$$

$R_{i|j}$ is the radial position of the $i|j$ interface, and is approximately the mean of the radii R_i and R_j. Equation (7) was used to estimate the spatially-averaged compression at $t = 10$ min (figure 5.3) and the time series of figure 6 (plain lines).

A.2. Derivation of equation (2)

We start from the power-law description of the Laplace transform of the 3 D displacement field, as introduced in [28]:

$$\vec{\delta}_R(s) = -A(s) \cdot \left(\frac{R}{R_0}\right)^{1+B(s)} \vec{E}_R.$$

Noting from figure 2.3 that $R^2 = r^2 + z_0^2$ and $\delta_r(s) = \delta_R \sin(\theta)$, with $\sin(\theta) = \sin\left(\arctan(r/z_0)\right) = \frac{r/z_0}{\sqrt{1+(r/z_0)^2}}$, we obtain:

$$\vec{\delta}_r(s) = -A(s) \cdot \frac{r}{R_0}\left(\frac{r^2 + z_0^2}{R_0^2}\right)^{\frac{B(s)}{2}} \vec{e}_r. \tag{8}$$

$\vec{E}_R$ is the unitary radial vector in the spherical coordinate system, and $\vec{e}_r$ the unitary radial vector in the FFOCT image. (See figure 2.2.) In the regime of weak perturbation ($B(s) \simeq 0$), we use a first order Taylor expansion of equation (8):

$$\vec{\delta}_r(s) \approx -\Big(A(s) \cdot r/R_0 + A(s) \cdot B(s) \cdot f(r)\Big)\vec{e}_r, \tag{9}$$

where $f(r) = \frac{r}{2R_0} \cdot \ln\left(\frac{r^2+z_0^2}{R_0^2}\right)$. Equation (9) writes as equation (2) in the temporal domain:

$$\vec{\delta}_r(t) \approx -\Big(\alpha(t) \cdot r/R_0 + \beta(t) \cdot f(r)\Big)\vec{e}_r.$$

Where $\alpha(t)$ and $\beta(t)$ are the inverse Laplace transforms of $A(s)$ and $A(s) \cdot B(s)$ respectively.

References

[1] Cheng G, Tse J, Jain R K and Munn L L 2009 *PloS One* **4** e4632
[2] Jain R K, Martin J D and Stylianopoulos T 2014 *Annu. Rev. Biomed. Eng.* **16** 321–46
[3] Stylianopoulos T *et al* 2012 *Proc. Natl Acad. Sci. USA* **109** 1510–78
[4] Engler A J, Sen S, Sweeney H L and Discher D E 2006 *Cell* **126** 677–89
[5] Heisenberg C P and Bellaïche Y 2013 *Cell* **153** 948–62
[6] Tse J M, Cheng G, Tyrrell J a, Wilcox-Adelman S a, Boucher Y, Jain R K and Munn L L 2012 *Proc. Natl Acad. Sci.* **109** 911–6
[7] Alessandri K *et al* 2013 *Proc. Natl Acad. Sci.* **110** 14843–8
[8] Mueller-Klieser W 2000 *Crit. Rev. Oncol./Hematol.* **36** 123–39
[9] Hirschhaeuser F, Menne H, Dittfeld C, West J, Mueller-Klieser W and Kunz-Schughart L a 2010 *J. Biotechnol.* **148** 3–15
[10] Montel F *et al* 2011 *Phys. Rev. Lett.* **107** 1–4
[11] Montel F, Delarue M, Elgeti J, Vignjevic D, Cappello G and Prost J 2012 *New J. Phys.* **14** 055008
[12] Delarue M, Montel F, Vignjevic D, Prost J, Joanny J F and Cappello G 2014 *Biophys. J.* **107** 1821–8
[13] Gonzalez-Rodriguez D, Guevorkian K, Douezan S and Brochard-Wyart F 2012 *Science* **338** 910–7
[14] Foty R A, Forgacs G, Pfleger C M and Steinberg M S 1994 *Phys. Rev. Lett.* **72** 2298–301
[15] Forgacs G, Foty R A, Shafrir Y and Steinberg M S 1998 *Biophys. J.* **74** 2227–34
[16] Marmottant P, Mgharbel A, Kfer J, Audren B, Rieu J P, Vial J C, van der Sanden B, Mare A F M, Graner F and Delano-Ayari H 2009 *Proc. Natl Acad. Sci.* **106** 17271–5
[17] Phillips H M and Steinberg M S 1978 *J. Cell Sci.* **30** 1–20
[18] Guevorkian K, Colbert M J, Durth M, Dufour S and Brochard-Wyart F 2010 *Phys. Rev. Lett.* **104** 1–4
[19] Desmaison A, Frongia C, Grenier K, Ducommun B and Lobjois V 2013 *PLoS One* **8** 4–13
[20] Jeong K, Turek J J and Nolte D D 2010 *J. Biomed. Opt.* **15** 1560–2281
[21] An R, Turek J, Matei D E and Nolte D 2013 *Appl. Opt.* **52** 300–9
[22] Nolte D D, An R, Turek J and Jeong K 2012 *Biomed. Opt. Express* **3** 2825–41
[23] Tan W, Oldenburg A L, Norman J J, Desai T A and Boppart S A 2006 *Opt. Express* **14** 7159–71
[24] Farhat G, Mariampillai A, Yang V X D, Czarnota G J and Kolios M C 2011 *J. Biomed. Opt.* **16** 070505–3
[25] Nahas A, Bauer M, Roux S and Boccara A C 2013 *Biomed. Opt. Express* **4** 2138–49
[26] Nahas A, Tanter M, Nguyen T M, Chassot J M, Fink M and Claude Boccara A 2013 *J. Biomed. Opt.* **18** 121514
[27] Sun C, Standish B and Yang V X D 2011 *J. Biomed. Opt.* **16** 043001–12
[28] Delarue M, Joanny J F, Jülicher F and Prost J 2014 *Interface Focus* **4** 20140033
[29] Dubois A, Grieve K, Moneron G, Lecaque R, Vabre L and Boccara C 2004 *Appl. Opt.* **43** 2874–83

[30] Schmitt J 1998 *Opt. Express* **3** 199–211
[31] Duncan D D and Kirkpatrick S J 2001 *J. Biomed. Opt.* **6** 418–26
[32] Kirkpatrick S J, Wang R K and Duncan D D 2006 *Opt. Express* **14** 11585–97
[33] Ko H J, Tan W, Stack R and Boppart S A 2006 *Tissue Eng.* **12** 63–73
[34] Sutherland R 1988 *Science* **240** 177–84
[35] Bonnet-Gonnet C, Belloni L and Cabane B 1994 *Langmuir* **10** 4012–21
[36] Monnier S, Delarue M, Delon A and Cappello G submitted
[37] Wells P N T and Liang H D 2011 *J. R. Soc. Interface* doi:10.1098/rsif.2011.0054
[38] Swift J *et al* 2013 *Science* **341** 1240104
[39] Desprat N, Richert A, Simeon J and Asnacios A 2005 *Biophys. J.* **88** 2224–33
[40] McDowell E J, Ellerbee A K, Choma M A, Applegate B E and Izatt J A 2015 *J. Biomed. Opt.* **12** 044008
[41] Chaudhuri O, Parekh S H, Lam W a and Fletcher D A 2009 *Nat. Methods* **6** 383–7